ARCHIVES
of
FOUNDRY ENGINEERING

ISSN (2299-2944)
Volume 2025
Issue 2/2

5 – 20

1/2

10.24425/afe.2025.153788

Published quarterly as the organ of the Foundry Commission of the Polish Academy of Sciences

Assessment of Thermal Conditions by Slow Solidification in Al Alloys and the Facility

P. Mikolajczak
Poznan University of Technology, Poland
Corresponding author: E-mail: Piotr.Mikolajczak@put.poznan.pl

Received 03.07.2024; accepted in revised form 22.10.2024; available online 17.04.2025

Abstract

Mold filling and casting solidification are determined by gravity driven natural convection. Also forced convection induced by rotating magnetic field influences castings microstructure. The investigations of flow effect on the aluminum casting alloys and silicon rich alloys were mainly conducted on simple cylindrical specimens and focused on the microstructure, composition and strength of electromagnetic field. Unfortunately, the temperature field in the specimens and facility were mainly omitted or not enough discussed. In the current study thermal conditions in a special facility for flow effect investigation were studied, in experimental and numerical manner, concerning Al-Si-Mg alloys with various compositions and different solid fraction curves. Solidification simulation has proven slow cooling and uniform temperature on the cross-section of the specimen and crucible, nearly uniform solidification time throughout the whole specimen, wide mushy zone and proper construction of the facility protecting electric coils. Temperature gradient and cooling rate, for alloys where almost all solid fraction and latent heat released close to solidus, were significantly higher at the solidus temperature than by liquidus, whilst in alloys where latent heat released evenly and closer to liquidus, were smoothly changing across sample and from liquidus to solidus temperature. Numerically simulated microstructure parameters like e.g. SDAS, grain size and fraction of primary phase in α-Al first alloy presented values similar and smoothly changing across specimen. It was proposed to calculate secondary dendrite arm spacing SDAS based on the specified time period, that could be responsible for melting some arms or creating new arms by dendrites, and next careful SDAS measurement across specimen was recommended. Tested facility and experimental procedure, developed for studying flow effect on the Al alloys microstructure, was proven to be very resistant to interference.

Keywords: Aluminum alloys, Slow solidification, Temperature field, Experimental facility and procedure, Solid fraction curve

1. Introduction

Aluminum casting alloys with its excellent strength-to-weight ratio, thermal conductivity and light weight were applied in automobile industry for production of e.g. wheels, transmission cases and engine blocks [1,2]. Also wrought Al alloys in a form such as plate, forging, extrusion are widely used in the marine applications and aerospace industries because of their excellent corrosion resistance, weldability, recycling and light weight [3-5].

Silicon and magnesium are two from main alloying elements applied in casting and wrought aluminum alloys [6,7] by different concentration leading to formation of Mg_2Si phase. In AA6063 alloys widely used in the structural applications, the Si content ranges from 0.35 to 1.3% with Mg ranging from 0.6 to 1.2%, whilst in casting aluminum alloy A356, the Si amounts 6.5-7.5% and Mg 0.25-0.45%. Beside composition, the physical properties and microstructure of Al alloys may vary significantly depending on temperature gradient, cooling rate, solidification velocity and melt flow especially near and in the mushy zone.

Al alloys for forging and extrusion were produced in Direct Chill (DC) [8] casting process by using crystallizers which ensure oriented mushy zone direction and controlled solidification velocity. Because of complex phenomena and occurring defects

like macro segregation and hot tearing in DC [9], improvements were looked for in application of low frequency electromagnetic field [10,11]. In foundry industry are conducted studies on effect of artificially induced flow and developed methods: control of melt convection by travelling magnetic field [12], electromagnetic field [13], electromagnetic processing of particles strengthened alloys [14], electromagnetic casting [15] and low frequency electromagnetic field [16]. The continuous developments are observed in melt conditioning (MC and HSMC) [17,18], thixoforming [19,20], rheocasting [21,22] and semisolid metal processing (SSM) [23].

The effect of forced convection induced by rotating magnetic field RMF on aluminum alloys was studied in directional solidification on AlSiFe alloys [24,25] and in opposite by low temperature gradient and low cooling rate on AlSiMgFeMn [26], AlCuSi [27], AlSiFe [28] and AlSiMn [29,30] alloys.

Application of electromagnetic stirring EMS was also studied for production of high quality silicon, e.g. for photovoltaic installations. The studies with EMS included: purification of Si from Al-Si melt [31], enrichments of primary silicon from Al-Si melt [32], silicon refining using Si-Sn melt [33], separation of silicon from Ti-Sn melt [34], separation of silicon from Al-Si alloy [35], refining Si from Si-Al melt [36], purification of Si from Sn-30Si alloy [37], silicon separation from hypereutectic aluminum-silicon [38], morphological evolution of Si [39], separation mechanism of primary silicon [40], boron removal from Al-30Si-10Sn melt [41], controlling segregation [42] and enhancing segregation behavior of impurity in Al-30Si alloy [43,44].

The investigations of flow effect on the aluminum alloys [26-30] and on the silicon [31-44] were mainly conducted on simple cylindrical specimens in the crucible enveloped by insulation and coils, where the effect was evaluated and focused on the microstructure variation with different alloy compositions and strength of electromagnetic field.

Unfortunately, the temperature field in the specimens, in the crucible, insulation, coils and in the cooling system were mainly omitted or not enough discussed. There is lack of information about temperature, cooling rate, temperature gradient, in samples and in the crucibles used. These thermal conditions might have significant effect on studied microstructures.

From by low cooling rate and low gradient conducted studies on aluminum alloys [26-30] and silicon preparation [31-33, 41-44], only [43] presented temperature field and flow field in the specimens, where by applied rotating magnetic field RMF the temperature in the sample was homogenized.

The aim of the current study is to investigate thermal conditions in the specimen, crucible and insulation, which were applied in the facility [45] and used in studies on different alloys [26-30] with methodology similar to [31-33,41-44]. The objective of the numerical simulation is to indicate: temperature field in specimen, crucible, insulation, and cooling system, parameters applied in microstructure evaluation like temperature gradient and cooling rate, proposition for improvements in methodology and construction of facility used.

For this purpose, an experiment was carried out on the solidification of six AlSiMg alloys with slow cooling, without the use of stirring by RMF, using the experimental methodology previously developed in [45] (Fig. 1a) and applied in [26-30]. Series of numerical simulations were carried out, which reproduced the conditions of the tested solidification process in order to assess the thermal conditions in the specimen and in the facility.

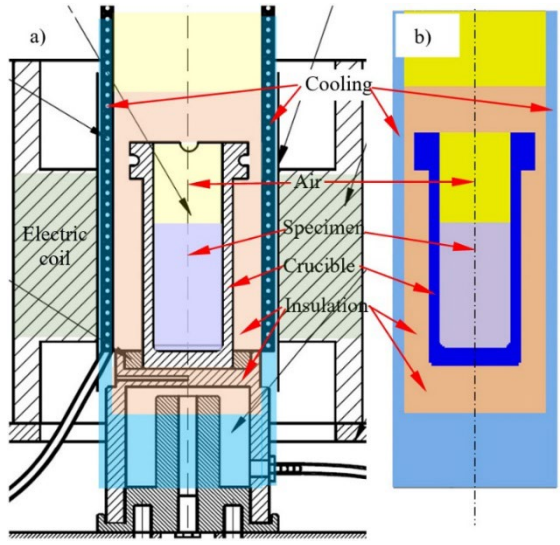

Fig. 1. The scheme of the tested facility: a) experimental facility, b) numerical model (mesh geometry)

2. Materials and methods

The methodology includes experimental specimens preparation and numerical simulation of the solidification and thermal conditions in specimens and in the facility used.

In the study, Al-Si-Mg alloys were studied, with variable composition around the eutectic point AlSi12.6Mg4.6 on the ternary phase diagram [46], with strictly controlled composition. The alloys were (Table 1): AlSi9.430Mg3.470 (labeled as "α-Al first" alloy), AlSi13.070Mg5.845 (labeled as "Mg_2Si first" alloy), AlSi14.180Mg4.400 ("Si first"), AlSi6.470Mg7.840 ("α-Al/Mg_2Si" alloy), AlSi12.515Mg2.250 ("α-Al/Si") and AlSi14.510Mg5.630 ("Mg_2Si/Si"). The chosen compositions made possible independent growth of some phase, e.g. in "α-Al first" alloy, the first independently growing phase is α-Al (L → α-Al + L) till final eutectic reaction (L → α-Al + Mg_2Si + Si) at 558.65 ˚C. Whilst in e.g. "Mg_2Si/Si" alloy joint growth of both Mg_2Si phase and Si crystals occurred (L → Mg_2Si + Si + L), till final eutectic reaction at 558.65 ˚C (L → α-Al + Mg_2Si + Si). Al the alloys were prepared from high purity materials, similarly to methodology in previous studies [26-30], were it was described in more details.

Table 1.
The studied AlSiMg alloys.

Name of alloy	Chemical composition	SDAS measured μm
"α-Al first"	AlSi9.430Mg3.470	54.8
"Mg_2Si first"	AlSi13.070Mg5.845	-
"Si first"	AlSi14.180Mg4.400	41.4
"α-Al/Mg_2Si"	AlSi6.470Mg7.840	-
"α-Al/Si"	AlSi12.515Mg2.250	67.7
"Mg_2Si/Si"	AlSi14.510Mg5.630	38.7

Solidification was conducted in the facility designed (Fig. 1) for studying the influence of rotating magnetic field RMF on the alloys structure [45]. The device owing set of coils may be powered from network via toroidal transformers in the three-phase system or via an autotransformer (Tufvassons, Sigtuna, Sweden, type KIEA 4), but RMF was not applied in the current study and alloys solidified by only natural convection, without electromagnetically generated forced convection. In order to control thermal conditions, thermocouples type K (TP-203) and the APAR AR 207 data recorder were applied. The winding of the coils located near to the casting and the crucible, were protected against heating using a cooler made of a copper tube (Fig. 1) in the form of a spiral, supplied with water (flow 5-10 L/min.). To provide slow solidification conditions in the 38 mm diameter and 67 mm long cylindrical specimens, the graphite crucible was surrounded by insulation with conductivity of about 0.1 W/mK (Fiberfrax, Unifrax, Tonawanda, USA). The construction of the device (Fig. 1) described in more detail in [45], allows for slow solidification at low cooling rate about 0.112 K/s and low temperature gradient about 0.143 K/mm. The graphite crucible has 38 mm inner diameter and 50 mm outer diameter (wall thickness 6 mm) by the whole high of 125 mm and was heated up in the smelting electric automatic furnace.

The specimens were first melted at 800 ˚C and then quickly moved together with the crucible into the facility where alloys slowly solidified, with temperature measurement and by natural convection, without application of rotating magnetic field.

The cut from specimens (Fig. 2) microsections were prepared with standard metallographic procedure, similarly to methodology in previous studies [26-30]. The samples were investigated with a microscope (Nikon Eclipse MA200, Japan) and allowed for secondary dendrite arm spacing λ_2 (labelled also as SDAS) measured as the averaged distance between 15-45 side branches.

Numerical simulations were conducted in Magmasoft [47]. Mesh geometry representing the used facility (Fig. 1) contains areas such as: specimen (light violet color) in the center, graphite crucible (dark blue color), insulation (orange) around and above crucible, air (yellow) in the crucible and above upper insulation, and finally cooling system (blue) outside and down. In the specimen and facility were placed thermocouples (green points on Fig. 2). Mesh geometry included 300 000 mesh cubes with dimensions about 1×1×1 mm. Thermophysical data for alloys was based on the Magmasoft [47] data base (AlSi10Mg, AlSi12-Sand, AlSi7Mg-Sand alloys) with modified by author chemical composition, thermophysical data and solid fraction curve. Solid fraction curves (Fig. 3) were determined from calculations in ThermoCalc [46] software. The studied alloys had significantly different precipitation sequence and amount of occurring phases, e.g. α-Al dendrites, Mg_2Si phases and Si crystals, which led to significantly different solid fraction curves and various intensity of latent heat release in liquidus-solidus temperature range. Thermophysical data for alloys used were: thermal conductivity (Lambda) 73-134 W/mK, density (Rho) 2095-2650 kg/m^3, specific heat (Cp) 910-1175 J/kgK. For graphite crucible were used data of the "Graphit" in Magmasoft data base: Lambda=52-116 W/mK, Rho=1800 kg/m^3, Cp=753-2095 J/kgK. Copper cooling system according to "Copper" in Magmasoft data base were: Lambda=180-400 W/mK, Rho=7400-8920 kg/m^3, Cp=385-515 J/kgK. Insulation was based on "Insulation" from Magmasoft data base, but modified according to data of Fiberfrax producer: Lambda=0.13-0.19 W/mK, Rho=390 kg/m^3, Cp=400-740 J/kgK. Boundary conditions between objects were: heat transfer coefficient C7000 (7000 W/m^{2}K) and default.air (1500 W/m^{2}K).

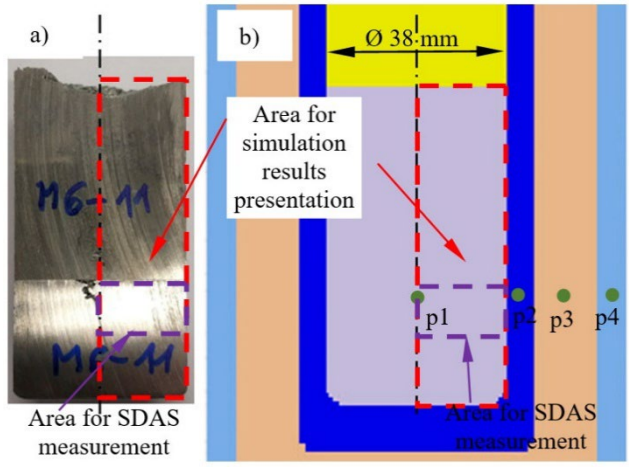

Fig. 2. Area for simulation results presentation (in red dashed line rectangle): a) experimental specimen, b) numerical model (with thermocouples – green points). Violet area selected for secondary dendrite arm spacing SDAS measurement

From initial analysis of thermal conditions in the specimen, crucible and cooling system, it was clear that most important is the proper value of the insulations thermophysical properties. Aluminum based specimen, copper cooling system and graphite crucible have quite high thermal conductivity, in comparison to insulation used. From all used materials, the insulation has the lowest thermal conductivity, and strongest determines the heat flow from specimen and crucible trough cooling system into environment. In order simplify the validation for experimental and simulated temperature curves compatibility, thermophysical data of other materials and boundary conditions were fixed, and Insulation properties were modified. Insulation the data were validated according to experimentally measured solidification time, and received well compatibility between experimental and simulated cooling curves as presented on Fig 4. Thermal conductivity (Lambda) for similar alloys was finally defined as: 0.1186 W/mK for α-Al first alloy, 0.1490 W/mK for Mg_2Si first alloy, 0.1171 W/mK for Si first first, 0.1380 W/mK for α-Al/Mg_2Si, 0.1152 W/mK for α-Al/Si and 0.1470 W/mK for Mg_2Si/Si alloy. As presented on the Fig 4a, the experimental and simulated temperature curves have very well compatibility in the temperature range 800-600 ˚C (time from 0 to 600 s) and also good compatibility for solidification time period (Fig. 4b). Thanks to validation, the heat flow in simulation was very well balanced according to experimental data.

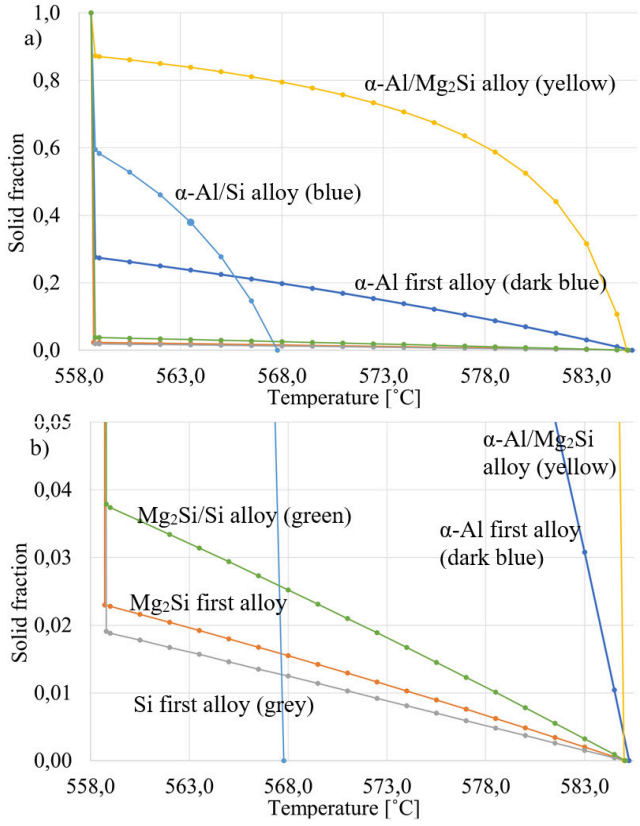

Fig. 3. Solid fraction fs curve in the studied alloys: a) fs in the range from 0 to 1, b) fs from 0 to 0.05

Initial temperature for specimen and crucible was 800 ˚C, and 11 ˚C for insulation, cooling system and the air. In the experiment, alloys were melted in the crucible during the heating up to 800 ˚C and then both moved into facility, and that is why no filling simulation was conducted, only solidification calculation.

Main question in the study is, if the experimental methodology [45] on studying influence of rotating magnetic field RMF on alloys microstructure [26-30], really occurs during slow solidification with equal thermal conditions in the whole specimen. The analyzes planned in the current study concerned: the temperature development during solidification, in the tested specimen and in the crucible, insulation, cooling system, with additionally determined temperature gradient, cooling rate, etc. In order to evaluate experimental process variables and proper construction of the device, following tests were conducted assessing effect of e.g. initial temperature of insulation (Fiberfrax) or initial temperature of the alloy and the crucible. Also the numerical prediction of solidification time and secondary dendrite arm spacing were of interest.

In the currently investigated microstructures, author studied phases well-known from previous works [26-30] and many other studies [48-50].

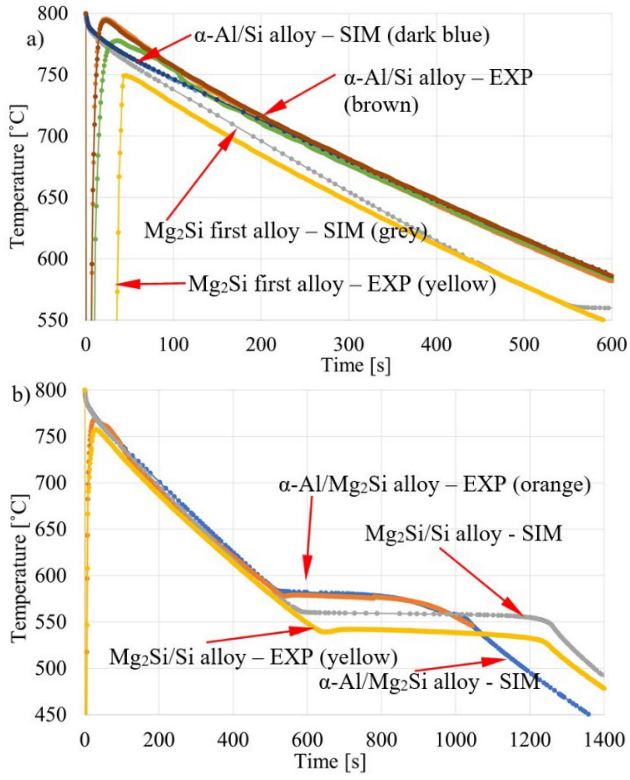

Fig. 4. Temperature curve measured in the crucible by experiment EXP and by simulation SIM, presented in the temperature range: a) from 800 to 600 ˚C, b) from 800 to 450 ˚C, for selected alloys

3. Results and Discussion

The results obtained from numerical simulation presented three main aspects of the investigated experimental methodology and achieved results by studying microstructures formed by slow solidification: a) thermal conditions in the specimen and facility, b) numerical prediction of secondary dendrite arm spacing SDAS, c) effect of experimental procedure on thermal conditions.

3.1. Thermal conditions in the specimen and in the facility

3.1.1. Temperature, solidification time and liquid fraction

Fig. 5 presents temperature in the specimen and in the facility (crucible, insulation, cooling) at the time: b) 600 s (0% of solidified specimen), c) 900 s (50%) and d) 1800 s for the α-Al first alloy. It seems that the temperature in the specimen and crucible are equal and very uniform, also in the cooling system temperature is uniform (blue color), whilst across the insulation temperature changes significantly.

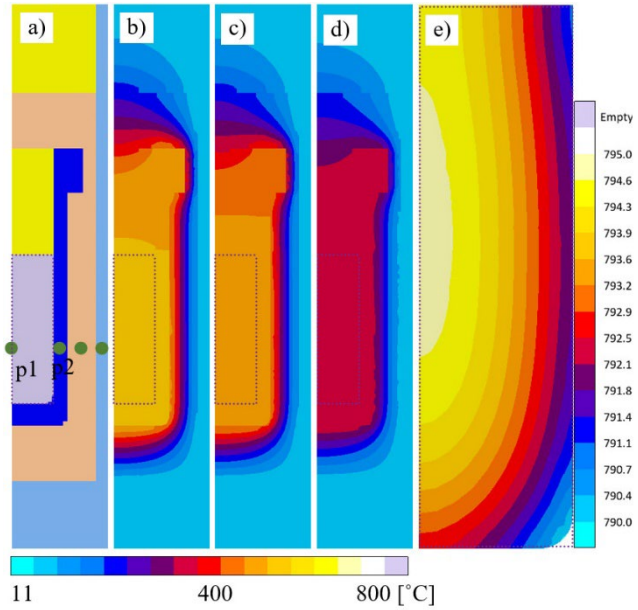

Fig. 5. a) Mesh geometry (with thermocouples – green points) and Temperature in the specimen and the facility (crucible, insulation, cooling) at the time: b) 600 s (0% solidified specimen, c) 900 s (50%) and d) 1800 s for the α-Al first alloy, e) temperature in the specimen only at the time 6.68 s and temperature range 790-795 ˚C in the whole specimen. The dashed line indicates the specimen on the figures a-d and also on figure e

Cooling curves (Fig. 6) measured in virtual thermocouples (green points p1 and p2 on Fig. 5a and 2b) located in specimen and crucible, confirms observations from Fig. 5 b-d, that specimen and crucible have almost equal temperature, and in the insulation (point p3, Fig 2b) temperature differs significantly from crucible and from cooling system (p4) during the whole time of the experimental process. Temperature (Fig. 6b) in the specimen center (p1) and in the crucible (p2, in the center of the 6 mm thick crucible wall), differs only about 3-4 ˚C during solidification. On the distance 22 mm (specimen radius 19 mm and 3 mm in the crucible), the simulated temperature gradient reaches about 0.13-0.18 ˚C/mm and confirms the low value of 0.143 ˚C/mm from experimental measurements [45]. Based only on this first results might be concluded that the conditions for slow solidification intended in [45] and used in [26-30] have been met.

Significant difference between temperatures in specimen, insulation and cooling system, as seen on Fig. 5 and 6, confirms proper effect of insulation applied and the cooling system and very well protection of the electric coils surrounding specimen (Fig. 1). In this way, it was proved that construction of the facility [45] was correctly designed. The Figures 5 and 6 confirmed also the correct methodology assumed in the current simulation, leading to validation by modification of only insulation thermophysical properties, working as the strongest thermal resistance by heat flow from specimen into the environment.

Simulated temperature curves (Fig. 7) measured in the specimen center (point p1 on Fig. 5a), vary significantly between studied alloys with strongly differentiating solid fraction curves (Fig. 3). In the α-Al/Mg_2Si alloy (Fig. 3a, yellow line), the latent heat begins to release significantly just after reaching liquidus temperature, and that caused slower cooling starting early in the process (at time 460-480 s, Fig. 7, grey color line) and in the higher temperatures (about 595 ˚C) . In the α-Al first alloy (Fig. 3a, dark blue line), the laten heat begins also to release just after reaching liquidus temperature, but less intensively as in α-Al/Mg_2Si alloy, and just before solidus temperature released only about 30% of solid phase and of latent heat. In the Si first alloy (Fig. 3b, grey line), the latent heat begins to release also just after reaching liquidus temperature, but very slowly and just before reaching solidus temperature released only about 2.0% of solid phase and latent heat. The rest of latent heat (about 98%) released by solidus temperature caused horizontal plain on cooling curve (Fig. 7, orange color) formed on the level close to solidus temperature. Different solid phase curves caused different cooling curves, but it might influence other thermal parameters and microstructure. Such an effect of the alloys composition and solid fraction curve was also observed on experimental cooling curves (Fig. 4).

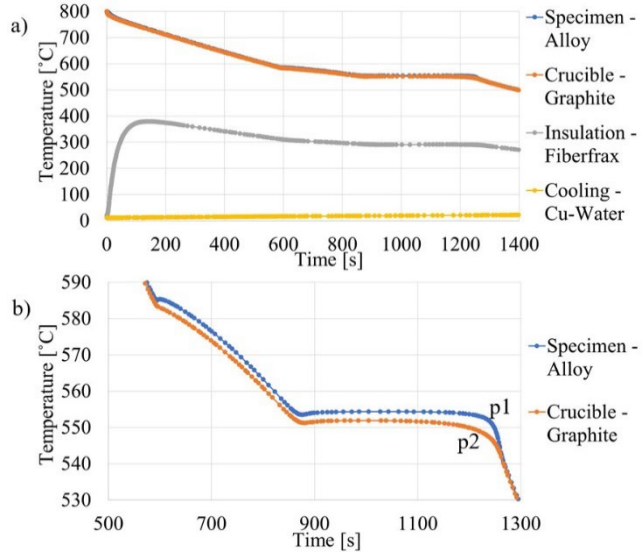

Fig. 6. Temperature curve measured by simulation of the α-Al first alloy, in the specimen center (alloy), in crucible, insulation and cooling, presented in the temperature range: a) from 800 to 0 ˚C, b) from 590 to 530 ˚C

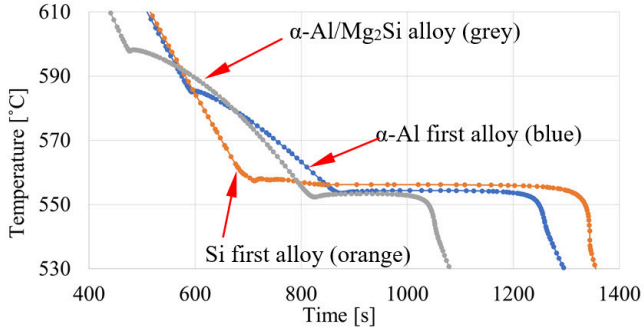

Fig. 7. Temperature curves measured by simulation, in the specimen center (alloy), in alloys with strongly differentiating solid fraction curves (seen on Fig. 3)

In the current study, simulated temperature across specimen (Fig. 5e) is consistent with results by Zou [43] calculated in Comsol software for AlSi30 alloy. The 40 mm diameter and 50 mm long specimen was cooled from 850 ˚C, together with graphite crucible surrounded by insulation. Just after starting cooling from 850 ˚C (Fig. 2a in [43]), the maximum 844.0 ˚C and minimum temperatures 838.0 ˚C differed only by 6 ˚C in experiment without rotating magnetic field RMF, whilst in current study 5 ˚C (Fig. 5e) difference was observed (in Magmasoft), also just after starting cooling and solidification, at the time 6.68 s. Melt stirring induced with 5 mT and 15 mT RMF [43], homogenized alloy and reduced the temperature range to 838.0-841.5 ˚C (3.5 ˚C) and 836.5-839 ˚C (2.5 ˚C) respectively.

Separation of primary silicon from AlSi45 alloy by alternating electromagnetic field was experimentally and in simulation studied by Xue [40] during solidification in graphite crucible (28 mm inner diameter) insulated with refractory material. The temperature field on Fig 7b in [40] suggests almost horizontal temperature iso-thermal lines, and it is difficult to assess exactly the temperature range, but the difference between temperature in across specimen and between specimen center and crucible are about 0-5 ˚C, and that agrees well with current results (Fig. 5 b,c,d and Fig. 6b).

Yu [39] during electromagnetic directional solidification of hypereutectic Al-Si alloys, applied high-purity graphite crucible (inner diameter 20 mm and depth 90 mm), and from simulation received, temperature distribution shown almost even horizontal iso-thermal lines, suggesting equal temperatures across sample and in crucible. Because of directional solidification, the differences between upper and bottom part of sample were about 40 ˚C.

In the high purity and density graphite crucible (17 mm inner diameter, 65 mm length), Lv [35] studied effect of electromagnetic directional solidification of AlSi45 alloy on the Si separation, and from simulation results, temperature distribution (Fig. 6a in [35] between upper and bottom part was about 200 ˚C, but temperature isolines were almost horizontal, suggesting close temperatures across sample and crucible.

Figure 8 shows liquid fraction (labeled as Fraction liquid FL [%] in Magmasoft) in the α-Al first alloy specimen at the specified time and percent of the whole specimen solidified. Even by common cooling of the specimen and crucible (starting both from 800 ˚C) and leading to slow solidification, the mushy zone also moves from crucible into the center, but the width of the mushy zone (Fig. 8 b,c,d) is extensive and reaches more than the specimens radius 19 mm. When considering the horizontal specimens cross-section at some specified level, the difference in solidification time reaches only 10-20 s (Fig. 9), and from practical point of view by general solidification time about 950-1350 s, the specimen solidify across whole sample at almost same time. What is interesting, upper part of the specimen solidify slightly quicker, and the bottom is the last solidifying part. Such a solidification sequence presented by liquid fraction was confirmed by solidification time ST (Fig. 9), where e.g. for α-Al first alloy, the bottom solidified at 1253 s, while the upper part by 1115 s, and similar tendency was observed for other studied alloys. It means that cooling effect of the air above specimen is important, and also microstructure parameters might slightly differ in the bottom and upper part. The tendency to intensive cooling of the upper specimen part was indicated in [40], where heat flow (Fig. 7a) was oriented upwards trough specimen and next led trough graphite crucible. But generally, from Fig. 8 and 9, it can be concluded that solidification occurs slowly almost by the same time in the whole specimens volume, supporting evenly distributed microstructure, e.g. equiaxed dendritic α-Al in α-Al first alloy. The place that solidify as the last one is on the ¼ of the specimens high, and suits the place of secondary dendrite arm spacing SDAS measurement (Fig. 2). Based on solidification time, studied alloys might be divided into two groups, one group of alloys solidifying by about 950-1050 s, and the second one by 1100-1350 s.

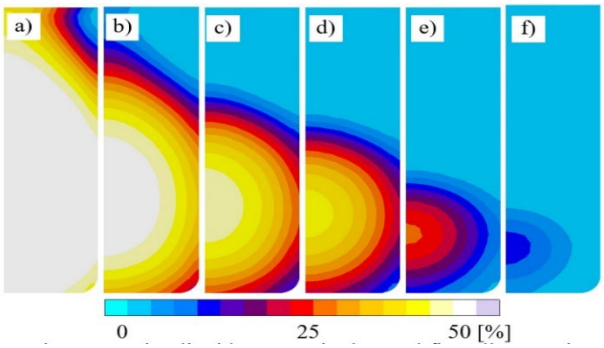

Fig. 8. Fraction liquid FL [%] in the α-Al first alloy specimen at the time (and percent of the whole specimen solidified): a) t=943 s, 50%, b) t=1047 s, 70%, c) t=1108 s, 80%, d) t=1146 s, 85%, e) t=1213 s, 95%, f) t=1245 s, 99%

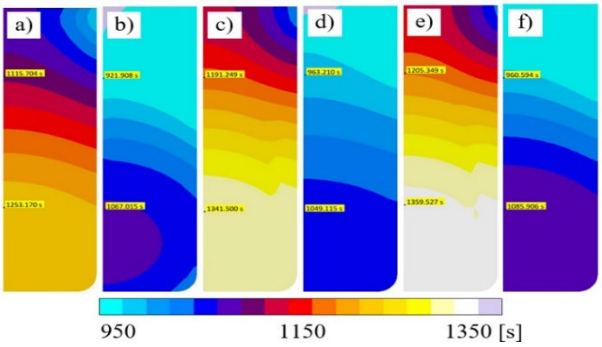

Fig. 9. Solidification time ST [s] in the specimen made of: a) α-Al first, b) Mg_2Si first, c) Si first, d) α-Al/Mg_2Si, e) α-Al/Si, f) Mg_2Si/Si alloy

3.1.2. Gradient time GT

Figure 10 presents temperature gradient (labeled in Magmasoft as Gradient time GT [˚C/mm]) in the α-Al first alloy specimen at the time and percent of the whole specimen solidified, at the same time as temperature presented on Fig. 8. It is important for interpretation knowing that, the parameter Gradient time GT shows gradient at a specific moment, e.g. at 943 s, when 50% of the whole specimen solidified (Fig. 10a). The value of gradient increases with solidification progress, and the higher values starts as first in upper part of specimen (Fig. 10a) and moves down (Fig. 10 b,c,d). Direct comparison between temperature (Fig. 8c) and gradient (Fig. 10b), can indicate that higher values of gradient are located in the area just after reaching solidus temperature. A similar observations follows from the comparison between figures 8d and 10c, and next between 8e and 10d, and also 8f and 10e. Gradient observed on the specimens bottom (blue colors Fig. 10 a, b, c) shows values from

0.08 to 0.15 ˚C/mm confirming experimental results 0.143 ˚C/mm from [45] and [26-30]. The consistency of results confirms the proper construction of the facility [45] and in current study correct validation by modifying insulation thermophysical data.

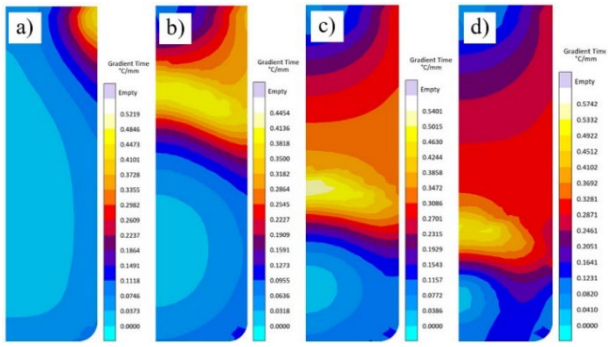

Fig. 10. Gradient time GT [˚C/mm] in the α-Al first alloy specimen at the time (and percent of the whole specimen solidified): a) t=943 s, 50%, b) t=1108 s, 80%, c) t=1213 s, 95%, d) t=1245 s, 99%

3.1.3. Gradient G and Cooling rate R

Next parameter characterizing thermal conditions, labeled as a Gradient G [˚C/mm], presents the temperature gradient in selected places in the specimen (in mesh cells) at the specified temperature (labeled as Thermo Criteria Temperature in Magmasoft). It is important for interpretation knowing that, in opposite to previously mentioned Gradient time GT, Gradient G (Fig. 11) calculated by liquidus temperature T_L (fs=0.00%) shows temperature gradient in different points (mesh cells in numerical simulations) at different times, but exactly when liquidus isothermal line comes through the point. Gradient G at liquidus (reaching values of 0.03-0.30 ˚C/mm) is very similar in the all studied alloys (Fig. 11), and this means that at the beginning of solidification, in the temperature range between initial 800 ˚C and liquidus, thermal conditions are similar in studied alloys and confirms results (0.143 ˚C/mm) obtained in studies [45] and [26-30]. For AlSi5Fe1.0 [26] alloy temperature gradient achieved $G_{800\text{-}liq} = 0.214$ (˚C/mm) and $G_{liq\text{-}470} = 0.143$ (˚C/mm), and for AlCu4Si6 [27] $G_{800\text{-}liq} = 0.196$ (˚C/mm) and $G_{liq\text{-}470} = 0.132$ (˚C/mm). In the upper specimens part, which solidified earlier than bottom (Fig. 9) gradient is slightly higher, but on specified horizontal cross-section, G is almost equal, and that confirms correct construction of the facility and experimental methodology.

Based on Fig. 10 and 8, suggesting higher gradient values by the end of mushy zone, gradient G [˚C/mm] was calculated (Fig. 12) by solidus temperature T_S (Thermo Criteria Temperature 558.6 ˚C) corresponding to solid fraction fs=100.0%. For α-Al first, α-Al/Mg_2Si and α-Al/Si alloys, G reaches values from about 0.03 to about 0.40 ˚C/mm, whilst for Mg_2Si first, Si first and Mg_2Si/Si alloys, G varies from 0.2 to 2.5 ˚C/mm, with highest values (e.g. 2.535 ˚C/mm pointed on Fig. 12c) located in the characteristically shaped area. On the chosen horizontal cross-section, in these Mg_2Si first, Si first and Mg_2Si/Si alloys, G differs significantly, and that influences thermal conditions for microstructure formation and precipitating phases, and finally may determine the results assessment in conducted experiments, similar to [26-30]. Also for vertical cross-section, G varies between upper and bottom part of specimen. What differs these two groups of alloys, is the completely different solid fraction curve (Fig 3), e.g. for second group of alloys (Mg_2Si first, Si first and Mg_2Si/Si), in overwhelming quantity, solid phase grows close to solidus temperature. It is clear that in these two groups of alloys, gradient G by solidus temperature was determined in different solidification manner, and the phases occurring in the microstructure, that grow at the end of solidification, had different thermal conditions and probably different parameters like SDAS, length, thickness or number density of precipitates (investigated in [26-30]).

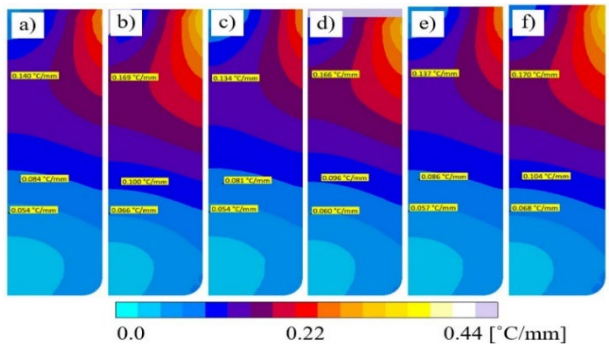

Fig. 11. Gradient G [˚C/mm] calculated by T_L (fs=0.00%) in the specimen made of: a) α-Al first, b) Mg_2Si first, c) Si first, d) α-Al/Mg_2Si, e) α-Al/Si, f) Mg_2Si/Si alloy

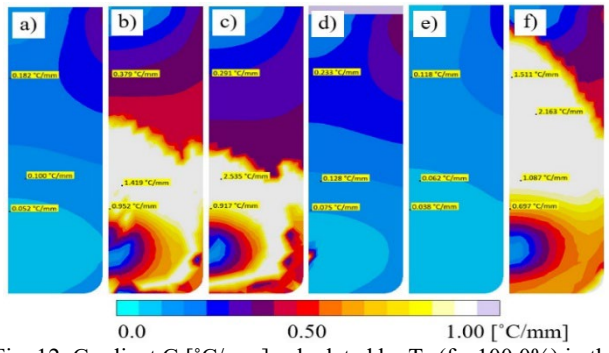

Fig. 12. Gradient G [˚C/mm] calculated by T_S (fs=100.0%) in the specimen made of: a) α-Al first, b) Mg_2Si first, c) Si first, d) α-Al/Mg_2Si, e) α-Al/Si, f) Mg_2Si/Si alloy

Gradient G calculated by liquidus temperature is similar for studied alloys (Fig. 11), whilst G calculated by solidus temperature (Fig. 12) differs and is strongly determined by solid fraction curve.

Cooling rate is the second important parameter (after gradient) characterizing thermal conditions. Cooling rate R [˚C/s] (Fig. 13) calculated by liquidus temperature T_L (fs=0.0%) shows more less equal values across each of specimens, by horizontal and vertical cross-sections. Here the alloys might be divided into two groups, one with R values of about 0.28-0.29 ˚C/s, and the second one with 0.33-0.37 ˚C/s. These results links to solidification time (Fig. 9).

Figure 14 shows Gradient G [˚C/mm] in the specimen made of Si first alloy, calculated at different solidification advancement, defined in Magmasoft with a Thermo Criteria Temperature, by the temperature (and solid fraction): a) 585.0 ˚C (0.0%), b) 578.4 ˚C (25%), c) 565.2 ˚C (75%), d) 558.6 ˚C (100%). Gradient G by solid fraction 0.0% and 25% reaches values 0.049-0.133 ˚C/mm, whilst

by 75% and 100% values 0.259-3.429 ˚C/mm, and is higher and more variable across specimen.

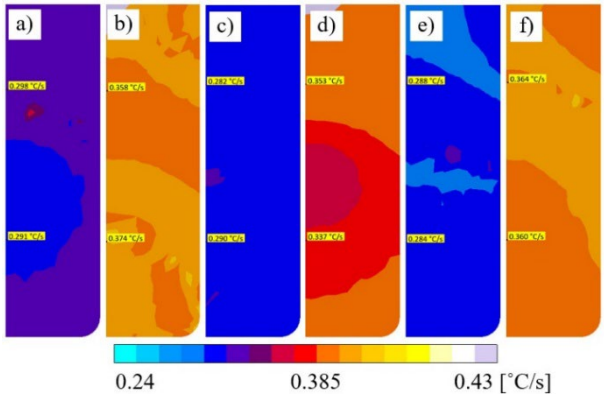

Fig. 13. Cooling rate R [˚C/s] calculated by T_L (fs=0.0%) in the specimen made of: a) α-Al first, b) Mg_2Si first, c) Si first, d) α-Al/Mg_2Si, e) α-Al/Si, f) Mg_2Si/Si alloy

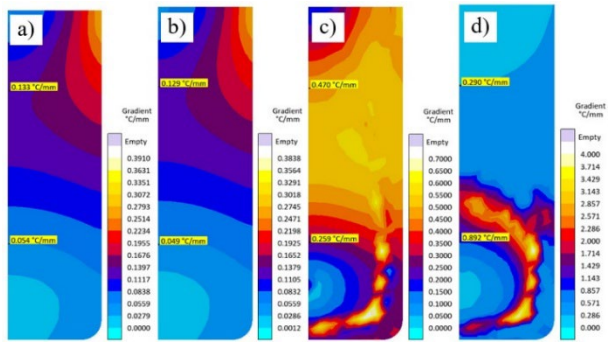

Fig. 14. Gradient G [˚C/mm] in the specimen made of Si first alloy and calculated by the Thermo Criteria Temperature (and solid fraction): a) 585.0 ˚C (0.0%), b) 578.4 ˚C (25%), c) 565.2 ˚C (75%), d) 558.6 ˚C (100%)

Similarly to gradient G, cooling rate R [˚C/s] (Fig. 15) in the specimen made of Si first alloy was calculated by the same Thermo Criteria Temperature (and solid fraction). For solid fraction 0.0%, 25% and 75%, cooling rate R reaches values from 0.09 to 0.290 ˚C/s, whilst for 100% is much higher, 0.069-9.40 ˚C/s and similarly to gradient G more variable across specimen.

Gradient G and cooling rate R for Si first alloy are significantly higher at the solidus temperature than by liquidus, the same as in Mg_2Si and Mg_2Si/Si alloys, where almost all solid fraction and latent heat release close to solidus temperature (Fig. 3b).

Figure 16 shows gradient G [˚C/mm] in the specimen made of α-Al/Mg_2Si alloy and calculated by the Thermo Criteria Temperature (and solid fraction): a) 585.0 ˚C (0.0%), b) 578.4 ˚C (25%), c) 565.2 ˚C (75%), d) 558.6 ˚C (100%) and reaches values from about 0.03 to 0.40 ˚C/mm, with higher values at the specimens top, and more or less smooth course across sample. The G values only slightly increase with increasing solid fraction, from 0.378 to 0.821 ˚C/mm in comparison to Si first alloy (Fig. 14).

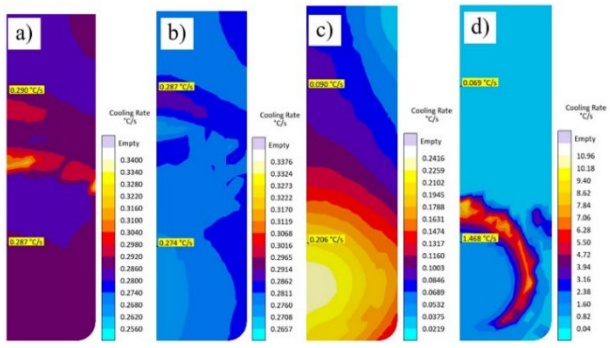

Fig. 15. Cooling rate R [˚C/s] in the specimen made of Si first alloy and calculated by the Thermo Criteria Temperature (and solid fraction): a) 585.0 ˚C (0.0%), b) 578.4 ˚C (25%), c) 565.2 ˚C (75%), d) 558.6 ˚C (100%)

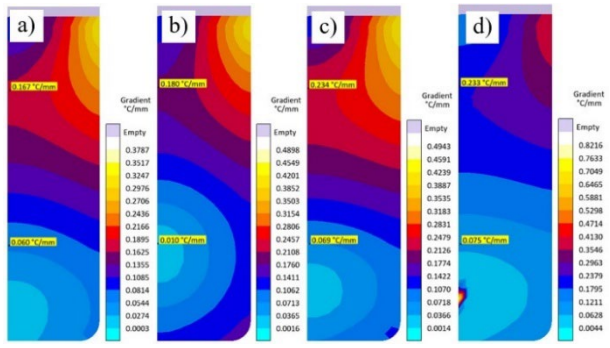

Fig. 16. Gradient G [˚C/mm] in the specimen made of α-Al/Mg_2Si alloy and calculated by the Thermo Criteria Temperature (and solid fraction): a) 585.0 ˚C (0.0%), b) 578.4 ˚C (25%), c) 565.2 ˚C (75%), d) 558.6 ˚C (100%)

Cooling rate R [˚C/s] (Fig. 17) in the specimen made of α-Al/Mg_2Si alloy was calculated by the same Thermo Criteria Temperature (and solid fraction) as gradient G. The R values are more or less smoothly changing across sample, e.g. for solid fraction 75%, in the range 0.129-0.186 ˚C/s. The lowest values are for solid fraction 25%, and the highest by 0%. By the 0.0% (Fig. 3a, yellow color line) no latent heat extracted yet, but by 25% (temperature 578.4 ˚C) extracted about 60% percent of heat.

In the comparison to Si first alloy (Fig. 14-15), in the α-Al/Mg_2Si alloy (Fig. 16-17), gradient G and cooling rate R smoothly changes across specimen and between different solidification advancements (solid fractions, Thermo Criteria Temperature). In the Si alloys some extremes occurred, related to solid fraction curve managing latent heat release.

The alloys composition leading to specified solid fraction curve, has influence on the variability in thermal conditions across specimens, may determine formation of occurring precipitates and should be taken into account when analyzing the resulting microstructures.

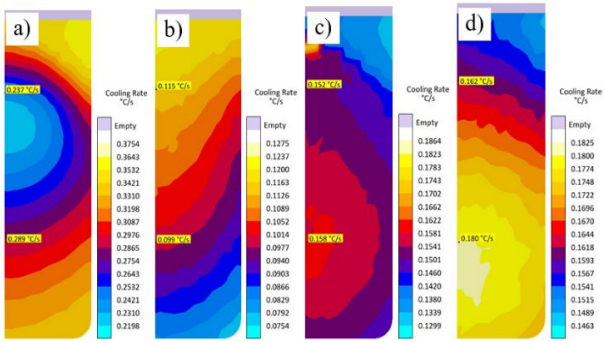

Fig. 17. Cooling rate R [°C/s] in the specimen made of α-Al/Mg_2Si alloy and calculated by the Thermo Criteria Temperature (and solid fraction): a) 585.0 °C (0.0%), b) 578.4 °C (25%), c) 565.2 °C (75%), d) 558.6 °C (100%)

3.2. Numerical prediction of secondary dendrite arm spacing SDAS

Numerical simulation allows for microstructure prediction like Fraction of primary phase in α-Al first alloy (Fig. 18a), Fraction of Mg_2Si phase in Mg_2Si first alloy (Fig. 18b), Fraction of eutectic phase in Si first alloy (Fig. 18c) or Grain size in α-Al first alloy (Fig. 18d). The values of the parameters are smooth across specimen (some, like Grain size are even equal), suggesting stable solidification conditions in the analyzed facility. The user has no possibility to influence the way of calculation of these parameters, and only can use it as the basis to build own parameters.

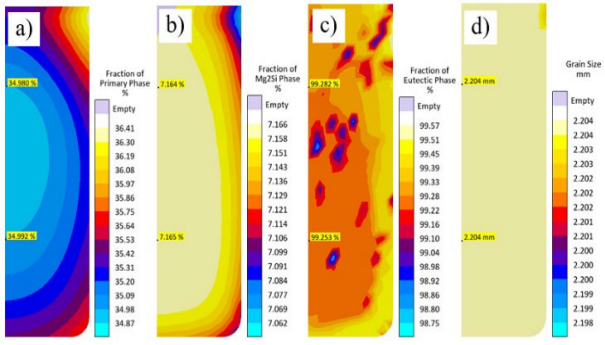

Fig. 18. Microstructure parameters available in Magmasoft: a) Fraction of primary phase in α-Al first alloy, b) Fraction of Mg_2Si phase in Mg_2Si first alloy, c) Fraction of eutectic phase in Si first alloy, d) Grain size in α-Al first alloy

Microstructure module in Magmasoft allows also for calculation of Secondary Dendrite Arm Spacing SDAS [μm] (Fig. 19) as presented for specimens made of: a) α-Al first, b) Si first, c) α-Al/Si and d) Mg_2Si/Si alloys. In specimens bottom, the printed values, e.g. 70.948 (Fig. 19a) for α-Al first alloy, are higher than that measured (Fig. 2, in violet rectangle area) in experiment, e.g. 54.8 (Table 1) μm for α-Al first alloy. Generally in the upper part, predicted SDAS seems to be lower, e.g. 66.183 μm for α-Al first alloy. But when analyzing SDAS on the horizontal cross-section, the values are in the range from 69.40 to 70.28, similar or even the same, and indicate nearly equal solidification conditions in the facility and even microstructure.

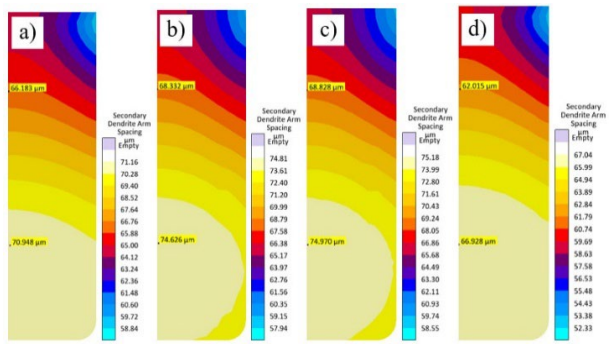

Fig. 19. Secondary Dendrite Arm Spacing [μm] calculated using Microstructure module in Magmasoft, in the specimens made of: a) α-Al first, b) Si first, c) α-Al/Si and d) Mg_2Si/Si alloy

Beside above mentioned Microstructure module, Magmasoft allows also for prediction of secondary dendrite arm spacing (SDAS) $\lambda_2 = \lambda_{SDAS}$ based on the equation:

$$\lambda_2 = c_1 \cdot (tS - tL)^{n_1} \quad (1)$$

where c_1 and n_1 are coefficients, by default c_1=11.03 and n_1=0.33 in Magmasoft. Fig. 20 shows such predictions in the specimens made of: a) α-Al first, b) Si first, c) α-Al/Si and d) Mg_2Si/Si alloy. Also in this case, the calculated values are higher (94.115 μm) than that measured in experiment, e.g. 54.8 (Table 1) μm for α-Al first alloy. Generally in the upper part, predicted SDAS seems to be lower, e.g. 87.746 μm for α-Al first alloy. When analyzing SDAS from the sample center to the crucible surface, the values are similar, and indicate nearly equal solidification conditions.

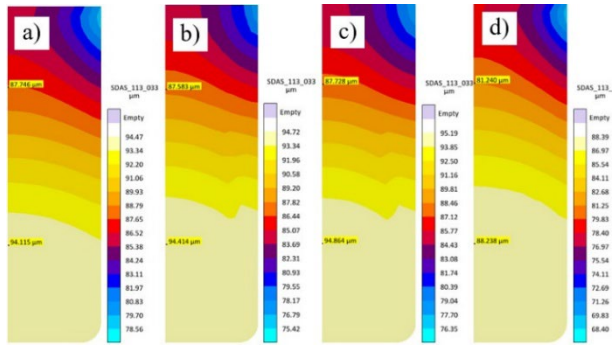

Fig. 20. Secondary Dendrite Arm Spacing [μm] based on t_S-t_L, c_1=11.03 and n_1=0.33 coefficients, in the specimen made of: a) α-Al first, b) Si first, c) α-Al/Si and d) Mg_2Si/Si alloy

The coefficient c_1 is materials depending. Fig. 21. shows Secondary Dendrite Arm Spacing [μm] based on equation (1), with n_1=0.33 and optimized value of c_1 coefficient, e.g. in the specimen made of α-Al first alloy, it amounts c_1=6.42 (Table 2). The optimized predictions (Fig. 21) shows also similar values across sample, and indicate nearly equal solidification conditions in the specimen.

Dendritic phases form, because close to the dendrite tip of main root, occurring perturbations in temperature and composition led to formation of cell-like structures, that later might form independent arms growing parallel. The occurring during solidification coarsening process seems to determine distance between secondary arms $\lambda_2 = \lambda_{SDAS}$ [51,52]. The assumption, that dendritic arms coarsening depends on diffusion, allowed for models discussed by Stefanescu [53], Kattamis [54], Rappaz [55] and Bouchard [56] based on the local solidification time t_S:

$$\lambda_2 = c_1 \cdot (tS)^{n_1} \quad (2)$$

where classically $n_1 = 0.33$ is for the diffusive regime [57] (0.48 for convective mass transport) and c_1 is materials coefficient [53-54,56,58-60].

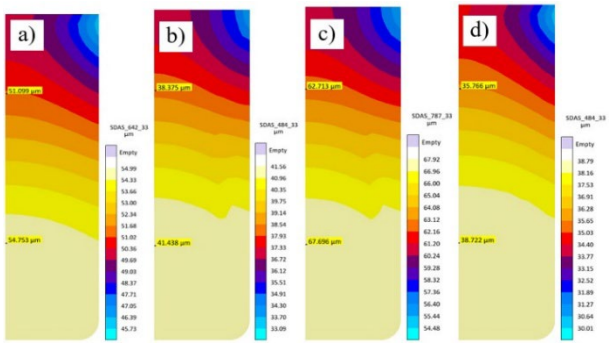

Fig. 21. Secondary Dendrite Arm Spacing [µm] based on t_S-t_L, n_1=0.33 and optimized c_1 coefficient, in the specimen made of: a) α-Al first (c_1=6.42), b) Si first (c_1=4.84), c) α-Al/Si (c_1=7.87) and d) Mg_2Si/Si alloy (c_1=4.84)

Fig. 22. shows Secondary Dendrite Arm Spacing [µm] based on solidification time t_S only, c_1=11.03 and n_1=0.33 coefficients, in the specimen made of: a) α-Al first, b) Si first, c) α-Al/Si and d) Mg_2Si/Si alloys, and the predicted values are higher than experimental. After optimization, for the compatibility between experimental (Table 1) and simulation SDAS values, by the materials coefficient c_1=5.20 (Table 2) for α-Al first alloy, the numerical prediction shows also similar values across sample (Fig. 23), and indicate equal solidification conditions in the facility.

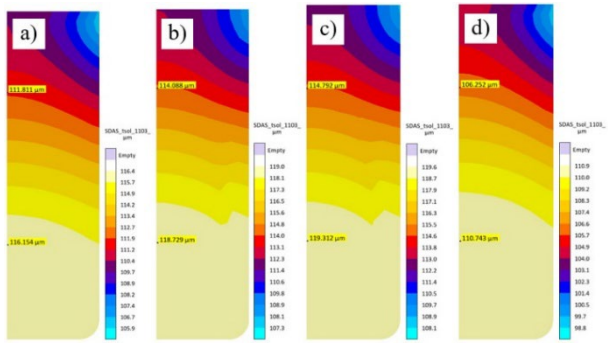

Fig. 22. Secondary Dendrite Arm Spacing [µm] based on t_S only, c_1=11.03 and n_1=0.33 coefficients, in the specimen made of: a) α-Al first, b) Si first, c) α-Al/Si and d) Mg_2Si/Si alloy

Table 2.
Secondary Dendrite Arm Spacing SDAS calculated by different formulas and c_1 coefficients (from literature or optimized) for selected alloy specimens

SDAS [µm]		Alloys			
		α-Al first	Si first	α-Al/Si	Mg_2Si/Si
Experimental		54.8	41.4	67.7	38.7
Simulated					
SDAS = c_1 * (t_S-t_L)^n_1	c_1=11.0	94.1	94.4	94.9	88.2
	c_1= …	(6.42)	(4.84)	(7.87)	(4.84)
		54.8	41.4	67.7	38.7
SDAS = c_1 *(t_S)^n_1	c_1=11.0	116.1	118.7	119.3	110.7
	c_1= …	(5.20)	(3.85)	(6.26)	(3.85)
		54.8	41.4	67.7	38.7
SDAS = c_1 * (t_S-t_X)^n_1	T_X= …	[565.2]	[559]	[560.9]	[559]
	c_1=11.0	37.0	16.93	39.83	16.51
	c_1= …	(16.33)	(26.97)	(18.75)	(25.85)
		54.8	41.4	67.7	38.7

(…) in the curly brackets the value of c_1 coefficient,
[…] in the square brackets the temperature T_X reached at the calculated time t_X.

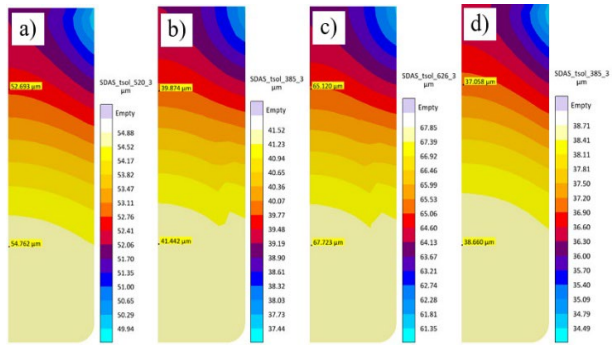

Fig. 23. Secondary Dendrite Arm Spacing [µm] based on t_S only, n_1=0.33 and optimized c_1 coefficient, in the specimen made of: a) α-Al first (c_1=5.20), b) Si first (c_1=3.85), c) α-Al/Si (c_1=6.26) and d) Mg_2Si/Si alloy (c_1=3.85).

According to the studies concerning the dendritic growth [51-60], the secondary dendrite arms grow during the whole solidification process in hypoeutectic AlSi alloys, but the spacing is determined mostly at the end of solidification, when some arms grow up and some melt and disappear. It was currently proposed to calculate SDAS based on the time period, that could be responsible for melting some arms or creating new arms. In the current study was assumed, that this process occurs in the last 25% of the temperature range, e.g. from temperature t_X=565.2 till solidus 558.6 ˚C in α-Al first alloy. Then proposed calculation of secondary dendrite arm spacing $\lambda_2 = \lambda_{SDAS}$ is based on the equation:

$$\lambda_2 = c_1 \cdot (tS - tX)^{n_1} \quad (3)$$

where t_X=565.2 ˚C. Fig. 24. shows SDAS [μm] based on t_S-t_X, n_1=0.33 and optimized c_1 coefficient (Table 2), in the specimens made of: a) α-Al first (t_X= 565.2 ˚C, c_1=16.33), b) Si first (t_X= 559.0 ˚C, c_1=26.97), c) α-Al/Si (t_X= 560.9 ˚C, c_1=18.75) and d) Mg_2Si/Si alloys (t_X= 559.0 ˚C, c_1=25.85). Of course, after c_1 optimization (Table 2), the values in the bottom part are equal to measured in the experiment, e.g. 54.8 (Table 1) μm for α-Al first alloy (Fig. 24 a). But surprisingly, in opposite to previous calculations using equations (1), (2) and simulations (Fig. 19-23), SDAS changes significantly on vertical cross-section, from the sample center to the crucible, from 54.833 to 77.67 μm (Fig. 24 a), increasing about 42%. This indicate and alarm, that in studied specimens, SDAS should be carefully and thoroughly measured across the sample (like in violet rectangle area presented on Fig 2). Such tendency was also for other alloys observed (Fig. 24 b,c,d), but in these α-Al/Si, Si first and Mg_2Si/Si alloys, dendritic α-Al occurs only residually and only few dendrites were observed on the microstructures. The proposed new calculation based on the shorter time period t_S-t_X instead of t_S-t_L or on only solidification time t_S, needs more experimental and numerical investigations.

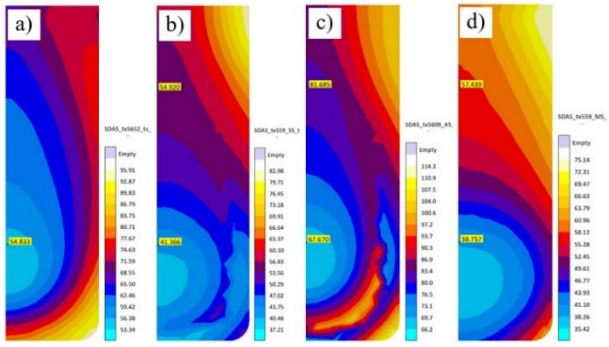

Fig. 24. Secondary Dendrite Arm Spacing [μm] based on ts-t_X, n_1=0.33 and optimized c_1 coefficient, in the specimen made of: a) α-Al first (t_X= 565.2 ˚C, c_1=16.33), b) Si first (t_X= 559.0 ˚C, c_1=26.97), c) α-Al/Si (t_X= 560.9 ˚C, c_1=18.75) and d) Mg_2Si/Si alloy (t_X= 559.0 ˚C, c_1=25.85)

3.3. Effect of experimental procedure on thermal conditions

For studying flow effect on the microstructure [26-30], many experiments on various alloys were conducted. During this experimental procedure [26-30, 45] some errors and threats may occur, e.g. improper value of initial temperature of alloy and crucible, e.g. 805 ˚C instead of 800 ˚C. Results in Tables 3-13 illustrate the effect of such conditions on the solidification time of the specimens. The solidification experiments were conducted only without rotating magnetic field, but may be usefully to asses thermal conditions.

The increase in the initial temperature of insulation (Fiberfrax) from 20 to 270 ˚C (Table 3) caused increase in solidification time 38 s and 33 s for Si first and α-Al/Mg_2Si alloy respectively. After first experiment ending with 270 ˚C, follows the next one, with the initial temperature 270 ˚C. The result presented, shows the risk, when by the first experiment, the insulation would not be heated up to 270 ˚C, or the interval between subsequent experiments would assume different values.

The increase in initial temperature of melt alloy and graphite crucible from 800 to 850 ˚C (Table 4) caused increase in solidification time 109 s and 103 s for Si first and α-Al/Mg_2Si alloy respectively. In the experiment, initial temperature is strictly controlled, and really may differ maximally 5 ˚C causing 12 or 10 s (Tab. 4) longer solidification time, and this 5 ˚C change may be analyzed as a real risk for experimental results.

The increase in the alloys quantity from 201 g (by the specimen length 67 mm) to 262 g (Table 5) caused increase in solidification time 192 s and 149 s for Si first and α-Al/Mg_2Si alloys respectively. The changes in dimensions of the specimen 30% or 10% are less probable. Specimens are precisely cut and 5% change in the dimension is real because during melting and mixing, also some oxides and slag may occur which are removed on the graphite mixer, and the loss of the alloy may occur. 5% loss of alloy may decrease solidification time 33 and 24 s for Si first and α-Al/Mg_2Si alloys respectively.

Table 3.
Solidification time [s] in function of initial temperature of insulation (Fiberfrax)

Solidification time [s]	Initial temperature of insulation			
	20 ˚C	100 ˚C	200 ˚C	270 ˚C
Si first alloy	1341	1351	1367	1379
α-Al/Mg_2Si alloy	1049	1057	1071	1082

Table 4.
Solidification time [s] in function of initial temperature of the alloy and the crucible

Solidification time [s]	Initial temperature of the alloy and the crucible				
	750˚C	795 ˚C	800 ˚C	805 ˚C	850 ˚C
Si first alloy	1206	1327	1341	1353	1450
α-Al/Mg_2Si alloy	935	1037	1049	1059	1152

Table 5.
Solidification time [s] in function of the alloys quantity and specimens length

Solidification time [s]	The alloys quantity						
	Specimens standard mass 0.201 kg and length 67 mm						
	141 g 46.9 mm (-30%)	181 g 60.3 mm (-10%)	191 g 63.5 mm (-5%)	201 g 67.0 mm (0%)	211 g 70.3 mm (+5%)	221 g 73.7 mm (+10%)	262 g 87.1 mm (+30%)
Si first alloy	1127	1270	1308	1341	1377	1411	1533
α-Al/Mg_2Si alloy	893	998	1025	1049	1074	1100	1198

10 ˚C increase or decrease in liquidus temperature (Table 6) almost do not changes the solidification time. The composition of the alloys was precisely calculated and components precisely

weighted. Supposing 0.3% error in the alloys composition, the change in liquidus temperature reaches 2 ˚C, and its effect on solidification time is insignificant.

The increase in initial temperature of copper cooling system from 11 to 91 ˚C (Table 7) caused increase in solidification time 169 s and 131 s for Si first and α-Al/Mg_2Si alloys respectively. Such a situation is only possible by the unnoticed lack of water from supply network. The really changes are possible from 11 to 21 ˚C, meaning only 20 s longer solidification for Si first alloy and such an effect is negligible.

The increase in thermal conductivity of the graphite used for crucible, from 64 W/mK to 70.4 ˚C (Table 8) caused decrease in solidification time 4 s both for Si first and α-Al/Mg_2Si alloys and is negligible. The crucibles were purchased from different companies and may have different thermal conductivity by exact the same shape and dimensions. Additionally crucibles were many times used, strictly cleaned from previous specimen and wear out, and that may lead to changes in heat flow. The really 5% higher thermal conductivity causes only 3 s shorter solidification time and its effect is negligible.

Table 6.
Solidification time [s] in function of the alloys liquidus temperature

Solidification time [s]	Liquidus temperature of the alloy (standard liquidus temperature 585 ˚C)				
	575 ˚C (-10˚C)	583 ˚C (-2 ˚C)	585 ˚C (0 ˚C)	587 ˚C (+2 ˚C)	595 ˚C (+10˚C)
α-Al first alloy	1253	1253	1254	1254	1254

Table 7.
Solidification time [s] in function of the initial temperature of the cooling system

Solidification time [s]	The initial temperature of the cooling system			
	11 ˚C	21 ˚C	51 ˚C	91 ˚C
Si first alloy	1341	1361	1422	1510
α-Al/ Mg_2Si alloy	1049	1064	1111	1180

In the current study, alloy was melted in the graphite crucible and next both heated up to 800 ˚C were moved to the facility for slow cooling and slow specimens solidification. But in case when alloy would be poured into 20 ˚C cold crucible (Table 9), the solidification time would decrease from 1341 s and 1049 s to 95 s and 50 s for Si first and α-Al/Mg_2Si alloys respectively. This test shows only how efficient is the use of a heated up crucible for introduction of slow solidification leading to equiaxed dendritic microstructure.

Table 8.
Solidification time [s] in function of thermal conductivity of the graphite crucible.

Solidification time [s]	Thermal conductivity of the graphite crucible				
	57.6 W/mK (-10%)	60.8 W/mK (-5 %)	64 W/mK (0 %)	67.2 W/mK (+5%)	70.4 W/mK (+10%)
Si first alloy	1346	1342	1341	1338	1337
α-Al/Mg_2Si alloy	1054	1051	1049	1046	1045

In the experimental procedure, possible errors in one exceptional situation may occur at the one experiment, causing extreme error. Table 10 shows solidification time [s] in function of extreme configuration of parameters variation (concerned as separate in Tables 3-8, Fig. 25b), when all errors occurs during one experiment and in one the same direction, increasing or decreasing solidification time. It is clear that such extreme situation may lead to only small errors, +81 s (comparison between Fig. 25 a and b) or -43 s (Fig. 25 a and c). In case when additionally initial temperature increases to 270 ˚C (not only 100 ˚C as in Table 10), then solidification time may increase from 1254 to 1362 (Table 11, Fig. 25 a and d). The experimental procedure, developed and realized for studying flow effect during solidification applied in [26-30] and presented in [45] seems to be very resistant to interference.

Table 9.
Solidification time [s] in function of initial temperature of the crucible

Solidification time [s]	Initial temperature of the crucible	
	20 ˚C	800 ˚C
Si first alloy	95	1341
α-Al/Mg_2Si alloy	50	1049

Table 10.
Solidification time [s] in function of extreme configuration of parameters variation

Extreme configuration of parameters variation	The variation of the studied parameter		
	in -	no variation	in +
Initial temperature of insulation	20 ˚C	20 ˚C	100˚C
Initial temperature of the alloy and the crucible	795 ˚C (-5 ˚C)	800 ˚C	805 ˚C (+5 ˚C)
The alloys amount variation from standard mass 0.201 kg	191 g, (-5 %)	201 g	211 g (+5 %)
The variation of the alloys liquidus temperature from 585 ˚C	583 ˚C (-2 ˚C)	585 ˚C	587 ˚C (+2 ˚C)
The variation of the initial temperature of the cooling system	11 ˚C	11 ˚C	21 ˚C
The variation of the graphite crucible's thermal conductivity	67.2 W/mK (+5 %)	64 W/mK	60.8 W/mK (-5%)
Solidification time [s]	1211 (-43 s)	1254	1335 (+81 s)
(…) in the curly brackets the variation of the parameter in % or in unit.			

In the situation, when conducting experiments, in the series of about 20 experiments, the first experiment might be conducted by initial temperature of insulation 20 ˚C, a not 270 ˚C as during the whole series. Insulation heating up during experiment reaches

about 270 ˚C (as seen on Fig. 7a, grey color line), then solidification time may change 39 s (Table 12, Fig. 25 a and e). But generally, according to experimental procedure [45], also for the first experiment, the insulation in the facility will be heated up by mounting some replacement hot crucible.

As seen on the Fig. 8, 9 and 25, the upper part of the specimen solidify earlier than the bottom. In order to decrease the difference, might be possible to cover the crucible with graphite cup, by changing the hot air above liquid alloy into a graphite. In future construction modifications, the graphite cup might replace the upper insulation. As presented in Table 13, such modification led to growth in solidification time, but the difference between upper and bottom part changed only small (Fig. 25 f), and such a modification in design needs more analysis.

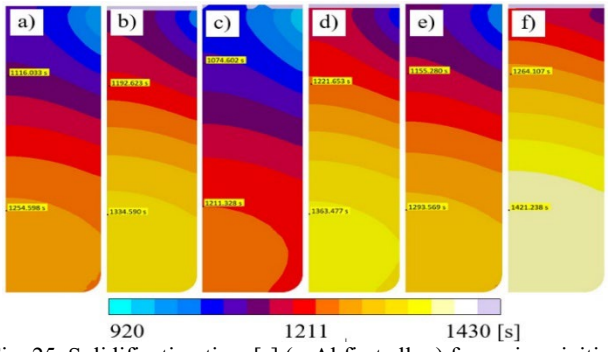

Fig. 25. Solidification time [s] (α-Al first alloy) for various initial, material, geometrical and boundary conditions testing possible variability of solidification conditions: a) standard version, b) max. possible solidification time increase, c) max. possible solidification time decrease, d) and additional effect of insulation initial temperature 270 [˚C], e) effect of the only change in the insulation initial temperature 270 [˚C], f) the change of air above the specimen into graphite cover

Table 11.
Solidification time [s] in function of initial temperature of the insulation

Solidification time [s]	Initial temperature of the insulation	
	20 ˚C	270 ˚C and other in + variations as in the Table 10
α-Al first alloy	1254	1362

Table 12.
Solidification time [s] in function of only initial temperature of the insulation

Solidification time [s]	Initial temperature of the insulation	
	20 ˚C	270 ˚C (as the only one variation)
α-Al first alloy	1254	1293

Table 13.
Solidification time [s] in function of material above the specimen (in crucible)

Solidification time [s]	The material above the specimen	
	Air (initial temperature 800 ˚C)	Graphite (initial temperature 800 ˚C)
α-Al first alloy	1254	1421

4. Conclusions

Experimental and numerical investigations on thermal conditions in AlSiMg alloys specimens and in the used facility, provided following observations and conclusions:

1. Slow cooling and nearly uniform temperature on the cross-section of the specimen and of the crucible has been proven,
2. Even values of solidification time throughout the specimen were observed,
3. The numerically tested construction of the facility provided proper electric coils protection and low stable temperature in the cooling system,
4. Temperature cooling curves significantly varied between alloys with different compositions and solid fraction curves,
5. A wide mushy zone running from the top of the sample and from the side walls was proven in simulation,
6. The area that solidifies in specimen as last one was located at a height of approximately ¼ of the specimen,
7. Higher gradient values for the mushy zone close to solidus temperature T_S for the α-Al first alloy were observed,
8. Temperature gradient and cooling rate, for Si first, Mg_2Si first and Mg_2Si/Si alloys were significantly higher at the solidus temperature than by liquidus, where almost all solid fraction and latent heat release close to solidus, whilst in α-Al/Mg_2Si, α-Al first and α-Al/Si alloys gradient and cooling rate were smoothly changing across sample and from liquidus to solidus temperature,
9. Temperature gradient and cooling rate strongly related to solid fraction curve managing latent heat release,
10. Numerically simulated microstructure parameters like e.g. SDAS, grain size and fraction of primary phase in α-Al first alloy presented values similar and smoothly changing across specimen. The calculated values of secondary dendrite arm spacing SDAS varied from obtained in the experiment and some optimization of the materials coefficient in the mathematical formula was necessary and helpful.
11. Based on proposed secondary dendrite arm spacing calculations based on the time period (assumed as last 25% of t_L-ts), that could be responsible for melting some arms or creating new arms by dendrites, and simulation results with occurred value changes on vertical cross-section, careful measurement of SDAS on the experimental specimens was recommended. The proposed formula for SDAS calculations needs more experimental and numerical analysis.
12. The analysis of the threats and errors that may occur in the experimental procedure concerned: changes in the initial temperature of insulation, melt alloy and crucible, cooling system, changes in the alloys quantity, liquidus temperature,

crucible conductivity, etc. and indicated small impact on experimental results.

13. The tested experimental procedure, developed and applied for studying flow effect during solidification seems to be very resistant to interference, and allows for proper analysis of the forced flow effect induced by rotating magnetic field, on the alloys microstructure.

Acknowledgements

The research leading to these results has received partial funding from the People Programme (Marie Curie Actions) of the European Union's Seventh Framework Programme (FP7/2007–2013) under the REA grant agreement n° PCIG13-GA-2013-613906. More information on the funded projects is available at: www.iFlowFePhase.info. This research was partially founded by the Ministry of Science and Higher Education in Poland, allocated at Poznan University of Technology, grant number 0613/SBAD/4888.

References

[1] Shwe, W.H.A., Kay, T.L. & Waing, K.K.O. (2008). The effect of ageing treatment of aluminum alloys for fuselage structure-light aircraft. World Academy of Science, Engineering and Technology. *International Journal of Materials and Metallurgical Engineering.* 2(10), 46, 696-699.

[2] Miller, W.S., Zhuang, L., Bottema, J., Wittebrood, A.J. & de Smet, P. (2000). Recent development in aluminum alloys for the automotive industry. *Materials Science and Engineering.* A 280, 37-49. https://doi.org/10.1016/S0921-5093(99)00653-X.

[3] The Aluminum Association, Inc. (1998). *Aluminum alloy selection and applications*. A monograph of Aluminum Association Incorporation, Washington, D C.

[4] Cubberly, W.H. (1979). *Properties and selection: non-ferrous alloys and pure metals.* Metals Handbook (Metals Park, OH: American Society for Metals).

[5] Smith, W.F. (1993). Alluminum alloys. In B.J. Clark andJack Maisel (Eds.), *Structure and properties of engineering alloys* (pp. 176-242). United States of America: McGraw-Hill Series.

[6] Mondolfo, L.F. (1976). *Aluminium Alloys: Structure and Properties*. London, UK: Butterworths & Co.

[7] Sarafoglou, P., I., Aristeidakis, J.S., Tzini, M-I. T. & Haidemenopoulos, G.N. (2016). Metallographic Index-Based quantification of the homogenization state in extrudable aluminum alloys. *Metals*. *6*(5), 121. doi: 10.3390/met6050121.

[8] Stefanescu, D. (1988). *The New Metals Hand Book: Casting,* ASM International.

[9] Eskin, D.G. & Katgerman, L. (2009). Solidification phenomena related to direct chill casting of aluminium alloys: fundamental studies and future challenges. *Materials Technology: Advanced Performance Materials.* 24(3), 152-156. DOI: 10.1179/106678509X12489478523537.

[10] Zhang, H., Nagaumi H. & Cui, J.Z. (2012). Effects of low frequency electromagnetic field of multi-physical fields during DC casting of 7xxx aluminum alloys. *Advanced Science Letters*. 13(1), 306-311(6). https://doi.org/10.1166/asl.2012.3762.

[11] Bojarevičs, A., Kaldre, I., Milgrāvis, M., Beinerts, T. (2017). Direct chill casting of aluminium alloys under electromagnetic. interaction. In VIII International Scientific Colloquium "Modelling for Materials Processing", 21-22 September 2017 (pp. 259-262). Riga. DOI: 10.22364/mmp2017.42.

[12] Zaïdat, K., Mangelinck-Noël, N., Moreau, R. (2007). Control of melt convection by a travelling magnetic field during the directional solidification of Al–Ni alloys. *Comptes Rendus Mecanique.* 335, 330-335. DOI: 10.1016/j.crme.2007.05.010.

[13] Patarić, A., Mihailović, M., Marković, M., Sokić, M., Radovanović, A. & Jordović, B. (2021). Microstructure as an essential aspect of EN AW 7075 aluminum alloy quality influenced by electromagnetic field during continuous casting process. *Hemijska industrija.* 75(1), 31-37. https://doi.org/10.2298/HEMIND201214006P.

[14] Kaldre, I., Milgravis, M., Bojarevics, A. & Beinerts, T. (2021). Electromagnetic processing during directional solidification of particle-strengthened aluminum alloys for additive manufacturing. *Materials Proceedings.* 3(1), 19, 1-4. https://doi.org/10.3390/IEC2M-09255.

[15] Patarić, A., Mihailovic, M. & Gulisija, Z. (2012). Quantitative metallographic assessment of the electromagnetic casting influence on the microstructure of 7075 Al alloy. *Journal of Materials Science.* 47, 793-796. DOI 10.1007/s10853-011-5855-3.

[16] Wang, X.J., Zhao, Z.H., Zuo, Y.B., Zhu, Q.F., Qu, F. & Cui, J.Z. (2009). Effects of low frequency electromagnetic field on solidification of 7050 aluminium alloy during hot top casting. *Materials Science and Technology*. 25(10), 1207-1210. https://doi.org/10.1179/174328408X382172.

[17] Sree Manu, K.M., Barekar, N.S., Lazaro-Nebreda J., Patel, J.B. & Fan, Z. (2021). In-situ microstructural control of A6082 alloy to modify second phase particles by melt conditioned direct chill (MC-DC) casting process – A novel approach. *Journal of Materials Processing Technology.* 295, 117170, 1-14. https://doi.org/10.1016/j.jmatprotec.2021.117170.

[18] Zhang, Y., Patel, J.B., Lazaro-Nebreda, J. & Fan, Z. (2018). Improved defect control and mechanical property variation in high-pressure die casting of A380 alloy by high shear melt conditioning. *The Journal of The Minerals, Metals & Materials Society*. 70, 2726-2730. https://doi.org/10.1007/s11837-018-3005-y.

[19] Brollo, G.L., Proni, C.T.W. & Zoqui, E.J. (2018). Thixoforming of an Fe-Rich Al-Si-Cu Alloy—thermodynamic characterization, microstructural evolution, and rheological behavior. *Metals.* 8(5), 332, 1-24. https://doi.org/10.3390/met8050332.

[20] Haga, T. & Suziki, S. (2001). Casting of aluminum alloy ingots for thixoforming using a cooling slope. *Journal of materials processing technology.* 118(1-3), 169-172. https://doi.org/10.1016/S0924-0136(01)00888-3.

[21] Eslami, M., Payandeh, M., Deflorian, F., Jarfors, A.E.W. & Zanella, C. (2018). Effect of segregation and surface condition

on corrosion of rheo-HPDC Al–Si alloys. *Metals*. 8(4), 209, 1-18. https://doi.org/10.3390/met8040209.
[22] Mohammed, M.N., Omar, M.Z., Al-Zubaidi, S., Alhawari, K.S. & Abdelgnei, M.A. (2018). Microstructure and mechanical properties of thixowelded AISI D2 tool steel. *Metals*. 8(5), 316, 1-16. https://doi.org/10.3390/met8050316.
[23] Wang, H., Davidson, C.J. & St. John, D.H. (2004). Semisolid microstructural evolution of AlSi7Mg during partial remelting. *Materials Science and Engineering: A.* 368(1-2), 159-167. https://doi.org/10.1016/j.msea.2003.10.305.
[24] Mikolajczak, P. & Ratke, L. (2013). Effect of stirring induced by rotating magnetic field on β-Al5FeSi intermetallic phases during directional solidification in AlSi alloys. *International Journal of Cast Metals Research.* 26(6), 339-353. https://doi.org/10.1179/1743133613Y.0000000069.
[25] Mikolajczak, P. & Ratke, L. (2011). Intermetallic phases and microstructure in AlSi alloys influenced by fluid flow. *The Minerals, Metals & Materials Society (TMS)*. 10, 9781118062173. https://doi.org/10.1002/9781118062173.ch104.
[26] Mikolajczak, P. (2017). Microstructural evolution in AlMgSi alloys during solidification under electromagnetic stirring. *Metals.* 7(3), 89, 1-16. https://doi.org/10.3390/met7030089.
[27] Mikolajczak, P. (2021). Effect of rotating magnetic field on microstructure in AlCuSi alloys. *Metals*. 11(11), 1804, 1-24. https://doi.org/10.3390/met11111804.
[28] Mikolajczak, P. (2023). Distribution and morphology of α-Al, Si and Fe-Rich phases in Al–Si–Fe alloys under an electromagnetic field. *Materials*. 16(9), 3304. https://doi.org/10.3390/ma16093304.
[29] Mikolajczak, P. (2023). Morphology and distribution of α-Al and Mn-rich phases in Al-Si-Mn alloys under an electromagnetic stirring. *Archives of Foundry Engineering*. 23(3), 74-87. DOI: 10.24425/afe.2023.146665.
[30] Mikolajczak, P. (2023). Flow effect on Si crystals and Mn-phases in hypereutectic and eutectic Al-Si-Mn alloys. *Archives of Foundry Engineering*. 23(4), 72-86. DOI: 10.24425/afe.2023.146681.
[31] Jie, J.C., Zou, Q.C., Wang, H.W., Sun, J.L., Lu, Y.P., Wang, T.M. & Li, T.J. (2014). Separation and purification of Si from solidification of hypereutectic Al-Si melt under rotating magnetic field. *Journal of Crystal Growth*. 399, 43-48. http://dx.doi.org/10.1016/j.jcrysgro.2014.04.003.
[32] Wenzhou, Y., Wenhui, M., Guoqiang, L., Haiyang, X., Li, S. & Dai, Y. (2014). Effect of electromagnetic stirring on the enrichment of primary silicon from Al-Si melt. *Journal of Crystal Growth*. 405, 23-28. http://dx.doi.org/10.1016/j.jcrysgro.2014.07.035.
[33] Ma, X., Lei, Y., Yoshikawa, T., Zhao, B. & Morita, K. (2015). Effect of solidification conditions on the silicon growth and refining using Si-Sn melt. *Journal of Crystal Growth*. 430, 98-102. http://dx.doi.org/10.1016/j.jcrysgro.2015.08.001.
[34] Zhu, K., Hu, J., Ma, W., Wei, K., Lv, T. & Dai, Y.(2019). Effect of solidification parameters and magnetic field on separation of primary silicon from hypereutectic Ti-85 wt.% Si melt. *Journal of Crystal Growth*. 522, 78-85. https://doi.org/10.1016/j.jcrysgro.2019.05.012.
[35] Lv, G., Bao, Y., Zhang, Y., He, Y., Ma, W. & Leu, Y. (2018). Effects of electromagnetic directional solidification conditions on the separation of primary silicon from Al-Si alloy with high Si content. *Materials Science in Semiconductor Processing.* 81, 139-148. https://doi.org/10.1016/j.mssp.2018.03.006.
[36] Yoshikawa, T. & Morita, K. (2005). Refining of Si by the solidification of Si-Al melt with electromagnetic force. *ISIJ International*. 45(7), 967-971. https://doi.org/10.2355/isijinternational.45.967.
[37] Huang, F., Zhao, L., Liu, L., Hu, Z., Chen, R. & Dong, Z. (2019). Separation and purification of Si from Sn-30Si alloy by electromagnetic semi-continuous directional solidification. *Materials Science in Semiconductor Processing*. 99, 54-61. https://doi.org/10.1016/j.mssp.2019.04.015.
[38] He, Y., Yang, X., Duan, L., Li, S., Chen, Z., Ma, W., Lv, G. & Xing, A. (2021). Silicon separation and purification process from hypereutectic aluminum-silicon for organosilicon use. *Materials Science in Semiconductor Processing*. 121, 105333, 1-11, 1-11. https://doi.org/10.1016/j.mssp.2020.105333.
[39] Jiang, W., Yu, W., Li, J., You, Z., Li, C. & Lv, X. (2018). Segregation and morphological evolution of Si phases during electromagnetic directional solidification of hypereutectic Al-Si alloys. *Materials*. 12(1), 10, 1-14. DOI: 10.3390/ma12010010.
[40] Xue, H., Lv, G., Ma, W., Chen, D. & Yu, J. (2015). Separation mechanism of primary silicon from hypereutectic Al-Si melts under alternating electromagnetic fields. *Metallurgical and Materials Transactions A.* 46, 2922-2932. DOI: 10.1007/s11661-015-2889-1.
[41] Sun, Jl., Zou, Qc., Jie, Jc. & Li, T. (2016). Separation of primary Si and impurity boron removal from Al-30%Si-10%Sn melt under a traveling magnetic field. *China Foundry.* 13(4), 284-288. https://doi.org/10.1007/s41230-016-6036-4.
[42] Zou, Q., Tian, H., Zhang, Z., Sun, C., Jie, J., Han, N. & An, X. (2020). Controlling segregation behaviour of primary Si in hypereutectic Al-Si alloy by electromagnetic stirring. *Metals*. 10(9), 1129, 1-13. https://doi.org/10.3390/met10091129.
[43] Zou, Q., Han, N., Zhang, Z., Jie, J., Xu, F. & An, X. (2020). Enhancing segregation behaviour of impurity by electromagnetic stirring in the solidification process of Al-30Si alloy. *Metals*. 10(1), 155, 1-11. https://doi.org/10.3390/met10010155.
[44] Ren, Z. & Junze, J. (1992). Formation of a separated eutectic in Al-Si eutectic alloy. *Journal of Materials Science*. 27, 4663-4666. https://doi.org/10.1007/BF01166003.
[45] Mikolajczak, P., Janiszewski, J., & Jackowski, J. (2019). Construction of the facility for aluminium alloys electromagnetic stirring during casting. In *Advances in Manufacturing II: Volume 4-Mechanical Engineering* (pp. 164-175). Switzerland: Springer International Publishing. https://doi.org/10.1007/978-3-030-16943-5_15.
[46] Thermo-Calc 4.1—Software (2024) *Package from Thermo-Calc Software AB*. Retrieved June 10, 2023, from www.thermocalc.se.
[47] MAGMA (2024). *Gießereitechnologie GmbH. Kackertstr. 16-18*. Retrieved June 5, 2024, from www.magmasoft.de.
[48] Gustafsson, G., Thorvaldsson, T. & Dunlop, G.L. (1986). The influence of Fe and Cr on the microstructure of cast. Al-Si-Mg alloys. *Metallurgical Transactions A.* 17, 45-52. https://doi.org/10.1007/BF02644441.

[49] Prakash S.P., Om P. & Devendra K. (2020). Structure and mechanical behavior of in situ developed Mg_2Si phase in magnesium and aluminum alloys – a review. *RSC Advances.* 10(61), 37327-37345. http://dx.doi.org/10.1039/D0RA02744H.
[50] Yan, F. (2013). *Development of high strength Al-Mg2Si-Mg based alloy for high pressure diecasting process*. PhD thesis. BCAST. Brunel University Uxbridge, UB8 3PH United Kingdom.
[51] Hunt, J.D. (2001). Pattern formation in solidification. *Science and Technology of Advanced Materials.* 2(1), 147-155. https://doi.org/10.1016/S1468-6996(01)00040-7.
[52] Hunt, J.D. & Lu, S.Z. (1996) Numerical modeling of cellular/dendritic array growth: Spacing and structure predictions. *Metallurgical and Materials Transactions A.* 27, 611-623. https://doi.org/10.1007/BF02648950.
[53] Stefanescu, D. (2009). *Science and engineering of casting solidification.* Boston, MA, USA: Springer. https://doi.org/10.1007/b135947.
[54] Kattamis, T.Z. & Flemings, M.C. (1965). Dendrite morphology. Microsegregation and Homogenization of low alloy steel. *Transactions of the Metallurgical Society of AIME.* 233(5), 992-999.
[55] Rappaz, M. & Boettinger, W. (1999). On dendritic solidification of multicomponent alloys with unequal liquid diffusion coefficients. *Acta Materialia.* 47(11), 3205-3219. https://doi.org/10.1016/S1359-6454(99)00188-3.
[56] Bouchard, D. & Kirkaldy, J.S. (1997). Prediction of dendrite arm spacing in unsteady- and steady-state heat flow. *Metallurgical and Materials Transactions B.* 28(4), 651-663. https://doi.org/10.1007/s11663-997-0039-x.
[57] Steinbach, S. & Ratke, L. (2007). The influence of fluid flow on the microstructure of directionally solidified AlSi-base alloys. *Metallurgical and Materials Transactions A.* 38, 1388-1394. https://doi.org/10.1007/s11661-007-9162-1.
[58] Mortensen, A. (1991). On the rate of dendrite arm coarsening. *Metallurgical Transactions A.* 1991, 22, 569-574. https://doi.org/10.1007/BF02656824.
[59] Voorhees, P.W. & Glicksman, M.E. (1984). Ostwald ripening during liquid phase sintering—Effect of volume fraction on coarsening kinetics. *Metallurgical and Materials Transactions A.* 15, 1081-1088. https://doi.org/10.1007/BF02644701.
[60] Ferreira, A.F., Castro, J.A. & Ferreira, L.O. (2017). Predicting secondary-dendrite arm spacing of the Al-4.5wt%Cu alloy during unidirectional solidification. *Materials Research.* 20(1), 68-75. https://doi.org/10.1590/1980-5373-MR-2015-0150.